Title: Mesoporous optically clear heat insulators for sustainable building envelopes

Authors: Amit Bhardwaj[1]†, Blaise Fleury[1]†, Bohdan Senyuk[1,2]†, Eldho Abraham[1,2]†, Jan Bart ten Hove[1]†, Taewoo Lee[1,2]†, Vladyslav Cherpak[1]†, and Ivan I. Smalyukh[1,2,3,4]*

Affiliations:

[1]Department of Physics, University of Colorado Boulder, Boulder, CO 80309, USA

[2]International Institute for Sustainability with Knotted Chiral Meta Matter (WPI-SKCM[2]), Hiroshima University, Higashi-Hiroshima, Hiroshima 739-8526, Japan

[3]Materials Science & Engineering Program, University of Colorado Boulder, Boulder, CO 80309, USA

[4]Renewable and Sustainable Energy Institute, National Renewable Energy Laboratory and University of Colorado Boulder, Boulder, CO 80309, USA

†These authors contributed equally, listed alphabetically by first name.

*Corresponding author. Email: ivan.smalyukh@colorado.edu

Abstract: Mesoporous materials exhibit highly controlled nanoscale structures, often templated by liquid crystalline assemblies of surfactants, with emergent and often designable physical properties. However, scaling their fabrication to be suitable for uses like envelopes of buildings is challenging. Here we describe fabrication of flexible square-meter-sized films and multi-centimeter-thick slabs made of three-dimensional spatial graphs of mesopore tubes having all structural features under 50 nanometers. Solution-based kinetic fabrication process templates growing networks of cylindrical surfactant micelles with thin tubes of polysiloxane forming gel networks and, upon replacing surfactants and solvents with air, yields lightweight materials with >99% visible-range optical transparency and ~10 mW $K^{-1}m^{-1}$ thermal conductivity. Such predesigned metamaterials enable transparent thermal barriers for wall-grade insulated glass units, square-meter window retrofits and unconcentrated solar thermal energy harnessing.

Main Text: Buildings are responsible for consuming ~ 40% of all generated energy globally, and much of that energy is wasted in the heating and cooling the building interior (*1-7*) because building envelopes commonly lack the ability to passively maintain temperature needed for the comfortable indoor environment. Windows of buildings leak much of the cooling/heating energy (*2-5*): despite constituting on average only ~8% (often ~30% in modern high-end homes) by area of the building envelopes, they are responsible for ~50% of the heat transfer (*2-5*). Approaches aiming to address this challenge involve transparent cellulose or silica aerogels and vacuum-insulated glass units, but their deployment is still challenged by issues like scaling limitations, seal integrity, and high manufacturing costs (*2-14*). Recently, cellulose-based aerogel films could be scaled in lateral dimensions while achieving optical characteristics acceptable for window retrofitting applications (*11*), albeit their thickness could not be scaled beyond several millimeters while retaining transparency, limiting the overall thermal resistance that could be achieved in window units and retrofits. The high nanometers-to-micrometer polydispersity of pores in conventional aerogels is the primary contributor to their hazy appearance, making it difficult for aerogels to meet the stringent optical requirements for applications in windows (*7-14*), as well as making them less effective as thermal barriers (*15, 16*). Despite the recent progress in meticulous nanoscale morphology control (*3-14*), the intrinsic limitations of conventional aerogels stem from the lack of well-defined length scale controlling pores to stay much smaller than both the wavelength of light and mean free path of air molecules at ambient conditions (~60 nm), as needed to achieve high optical transparency and low thermal conductivity of porous materials (*4*).

Mesoporous materials, including mesoporous silicas, have been developed to exhibit highly controlled monodisperse pores, which are often templated by lyotropic liquid crystalline mesophases or by kinetic processes involving mesoscale self-organization of micelles (*17-23*). However, such materials have not been reported to be manufactured on building-relevant scales. Similarly, the target physical properties like thermal insulation and optical transparency have not been systematically studied or optimized.

We report optically transparent, highly thermally insulating pre-engineered metamaterials made from mesopore networks of polysiloxane tubes as a viable alternative for window insulation (*24*). By tuning mesoscale structure and solid content, we achieved thermal conductivity of 10-12 mW K^{-1} m^{-1}, much lower than that of still air (~27 mW K^{-1} m^{-1}), as well as average visible-range light transmission >99% (much higher than <92% of glass) with the haze coefficient < 1%. We scaled production of these mesoporous optically clear heat insulators (MOCHIs) to square-meter lateral dimensions and slab thickness > 3 cm, to overall building-relevant scales, while retaining their thermal and optical properties. We fabricated wall-grade insulated glass units with thermal resistance $R \approx 2.64$ m^2 K W^{-1} (15 h ft^2 °F Btu^{-1}) and higher for geometric form-factors (thickness) comparable to that of conventional double pane windows, while also meeting stringent requirements for such glazing applications. Additionally, we demonstrated how such transparent insulation allows for efficient harnessing of unconcentrated solar thermal energy. MOCHI metamaterials could potentially help convert inefficient building envelopes into energy-generating autonomous power plants.

Fabrication of slabs and films of MOCHI metamaterials

By using an optimized procedure that leveraged the out-of-equilibrium self-assembly of surfactant molecules into graph-like networks, which then templated networks of thin nanotubes of polysiloxane to eventually yield our predesigned MOCHI metamaterials (Fig. 1C-J, figs. S1 and S2), we fabricated square-meter films and multi-centimeter-thick slabs (Fig. 1A, B, figs. S3

and S4, movies S1 and S2). Briefly, methyl trimethoxy silane (MTMS) was added to a solution of an aqueous cetylpyridinium chloride (CPCL) surfactant, followed by additions of glacial acetic acid to hydrolyze the silane. Tetramethyl ethylene diamine (TEMED) was used to cross-link the polysiloxane network (tables S1 and S2) (*24*). This mixture was transferred to a prefabricated mold, which was sealed and then kept in a closed chamber to complete gelation at 55 ^{o}C within 12 to 72 hours, for sample thicknesses of 0.5 to 37.5 mm, respectively (*24*). After removal from the mold, the polysiloxane hydrogels were washed with water and transferred to ethanol at 40^{o}C. Repeated washing with fresh/distilled ethanol completed the solvent exchange and removed the surfactant (*24*). Subsequent carbon dioxide (CO_2)-based supercritical drying replaced ethanol with CO_2 that was then exchanged with air within the mesoporous tubular networks after removal using a custom-built supercritical dryer (fig. S3F). The ensuing highly porous MOCHI metamaterials were pre-designed to have a polysiloxane solid content of only 5 to 15% by volume (Fig. 1, fig. S5), fabricated according to recipes shown in tables S1 and S2 (*24*).

Transmission electron microscopy (TEM) imaging and tomographic reconstruction (Fig. 1, C to F, fig. S1, and movies S3 and S4) confirmed that MOCHI were composed of graph-like networks of thin bicontinuous tubes of polysiloxane. The inner pore diameters were roughly twice the length of CPCL surfactant molecules, and their nanometer-scale thickness and density varied with porosity (Fig. 1, C to I) (*24*). Dimensions of outer inter-nanotube network pores were typically ~30 nm or less. The nanotube orientations exhibited weak orientational correlations with respect to the geometry of the slabs or films that was related to the symmetry-breaking at the fabrication-stage solvent exchange and drying (*24*).

The morphology of MOCHI (Fig. 1D) was much different from that of common aerogels that are typically composed of networks of interconnected particles like nanospheres and nanofibers with polydisperse pore dimensions spanning many orders of magnitude (*4-11*), often from nanometers to tens of micrometers. Controlling pore and nanoparticle dimensions in nanocellulose and silica aerogels has been instrumental for achieving desired properties (*4-11*), such as optical transparency. However, progress has been limited, and so far, thick slabs of transparent aerogels have not been reported. By exploiting the surfactant self-assembly into cylindrical micellar networks as a guiding mechanism for nano-templating polysiloxane, we define dimensions of inner pores of nanotubes, distances between them within the graph-like networks, as well as their large-scale partial orientational order and anisotropic properties (Figs. 1 and 2).

Optical, thermal, and other properties

Our MOCHI metamaterials were highly transparent (Figs. 1A,B and 2, figs. S6-S9, and movies S5 - S8), effectively behaving like "frozen air", in contrast to hazy conventional aerogels that are often referred to as "frozen smoke". Figure 2B illustrates dramatic differences between transmission of light incident obliquely on edge faces of MOCHI and conventional window glass, where glass is non-transparent for large incidence angles due to the large contrast between refractive indices of glass (1.52) and air (1.0003). Because the refractive index of MOCHI (1.025-1.030) nearly matched that of air, MOCHI remained highly transparent even at large incidence angles, Fig. 2A-D. The very small <0.03 difference between the indices of air and MOCHI as compared to that of glass (>0.5) also caused the net total measured reflection from two MOCHI-air interfaces to be ≈0.02%, much lower than the corresponding ~8% reflectivity value for a slab of glass (Fig. 2D, inset).

Furthermore, even the very low reflection from air-MOCHI interfaces disappeared when two slabs of MOCHI were pressed against each other to achieve optical contact (Fig. 2, E and F, and movie S2), which was easier to achieve than for glass because of the comparatively soft nature of MOCHI. As a result, > 99% of normally incident visible light was transmitted, with ≈99.7% visible-range transmission measured with the help of an integrating sphere (*24*). Transmittance remained high (>90%) even for incidence angles >70° and over the entire visible spectrum (Fig. 2B and F, fig. S6). Conventional laser cutting (inset of Fig. 2F, movie S7) allowed fabrication of multi-centimeter-thick slabs of MOCHI of arbitrary geometric shapes that could be invisibly tiled with other slabs through creating optical contacts (*24*).

The morphology of partially orientationally ordered polysiloxane nanotubes (Fig. 1D-G) led to optical birefringence in the range of (0.2 to 1.4) × 10^{-5} (Fig. 2C, fig. S8), with the optical monocrystal-like ordering maintained over meter-scale dimensions of slabs defined by the directionality of solvent exchange and drying (*24*). Birefringence increased with porosity and showed a trend different from that of the effective refractive index (Fig. 2C).

Periodically-modulated scattering of a laser beam traversing through the slab (insets of Fig. 2B and C, fig. S9A) vividly illustrates birefringence properties of these materials on large scales. The L_s~2.5 cm modulation period of scattered light corresponds to the beam's polarization state changes from linear to circular (strong scattering) and back to linear (weak scattering) caused by the MOCHI's macroscopic optical-monocrystal-like anisotropic properties. The phase difference between ordinary and extraordinary modes changed by π as the light traversed the distance corresponding to the ~2.5 cm-scale L_s (*24*), within which the beam's polarization state changes from linear to circular (strong scattering) and back to linear (weak scattering). This birefringence is inconsequential for the main envisaged applications of MOCHI as transparent thermal insulators but may find other applications, e.g. in polarizing optics. The very high visible-range optical transparency also yielded high color rendering index >99% (*24*), so that viewing through MOCHI preserved natural colors (fig. S9B).

Mesoporous morphology was key to enabling the thermal properties of MOCHI (Fig. 3A, figs. S10 - S12). Because the pores were much smaller than the mean free path between collisions of air molecules at ambient temperatures and pressures (60 to 70 nm), these molecules collide with the pore walls more often than with each other, so gas conduction of nanoconfined air was strongly inhibited. The tubular polysiloxane network of MOCHI was also a poor thermal conductor because of its geometric complexity, poor thermal contacts at tubular junctions, and small solid fraction by volume.

The interplay between the conduction contributions caused by the gas and solid network was generally more complex than for conventional aerogels with polydisperse random pores as MOCHI's inner pores of tubes were monodisperse and small (~5 nm), whereas the 20-30 nm inter-tube pores were controlled by porosity (Fig. 1C-H). These structural aspects may be a source of apparent two local minima on thermal conductivity versus porosity dependencies (Fig. 3A), albeit future studies will be needed to confirm this hypothesis. Furthermore, the polysiloxane within MOCHI strongly absorbed radiation in most of the thermal infrared range corresponding to blackbody radiation at ambient conditions (Fig. 3B). Thus, the radiative contribution to heat transfer through thick slabs of MOCHI was negligible because sequential processes of absorption and re-emission effectively led to thermal-range radiation bouncing back from the slab, consistent with our modeling of thermal resistance (fig. S13) and enabling high-R insulating glass units (IGUs) with high visible-range transparency (figs. S14-S18) (*24*).

Optimized-composition MOCHI were highly insulating, with thermal conductivity 10-12 mW K^{-1} m^{-1} at ambient temperatures (Fig. 3A) and thermal barrier properties useful for many applications (Figs. 3C-I and 4). MOCHI also exhibited mechanical robustness (fig. S19 and movie S9) and could be adhered to plastic films or glass substrates, which allowed for undergoing hundreds of rolling-unrolling (fig. S20) and heating-cooling cycles (fig. S21), as well as accelerated lifetime characterization within an IGU or a retrofit (*24*). Because of composition and large surface area of the mesoporous morphology, MOCHI were fire retardant (inset of Fig. 3A, movies S1 and S10), superhydrophobic and water repellant (inset of Fig. 1B, movie S6). These MOCHI properties persisted even after ~5 years of being adhered to an interior surface of a window, under dust fouling, chemical exposure and acid rain (figs. S21E,F, S22 and S23) (*24*).

Windows, skylights, solar thermal energy harnessing

The thermal resistance of 2.64 m^2 K W^{-1} (≈ 15 h ft^2 °F Btu^{-1}) of optimized MOCHI of 2.5cm slab thickness allowed for making window units insulated better than conventional building walls while having geometric form-factors (thickness) comparable to that of the common double-pane windows (Fig. 3C-I, figs. S14-S18 and tables S3-S5). Although relatively thin (3 mm) films of MOCHI could be rolled and super-critically dried for applications in large-area window retrofits (Fig. 1A), scaling of thick slabs was challenging as the cost of vessels capable of operating at the elevated pressures of CO_2-based super-critical drying is prohibitive for large samples. However, the ability of forming good "optical contact" between edge faces of MOCHI slabs (Fig. 2E and F, movie S2) or large-area films allowed for scaling the size of high-*R* MOCHI-IGUs made from overall laterally large and thick MOCHI slabs (Fig. 3C-I). These slabs could be laser-cut to various geometric shapes (inset of Fig. 2F, movie S7), providing the ability to make complex-shaped high-R IGUs (Fig. 3G) (*24*).

Because MOCHI effectively blocked thermal-range blackbody radiation under window-relevant conditions (Fig. 3B), high-R thermal insulation could be achieved even without using low-emissivity coatings on glass (Fig. 3C-I) (*24*), with experimentally measured *R*-values matching the results of computational modeling (fig. S17, table S5) (*24*, *25*). On the other hand, 3 to 4 mm thick MOCHI films adhered to the interior of single pane windows boosted their insulation to be comparable to that of double pane windows, with $R \approx 0.53$ m^2 K W^{-1} (3 h ft^2 °F Btu^{-1}).

As an additional benefit beyond energy efficiency, the use of MOCHI in IGUs and retrofits also boosts condensation resistance (fig. S21A) and soundproofing (fig. S24) as compared to conventional single- and double-pane windows (*24*). IGUs with ≈19mm and 25mm MOCHI slabs between panes reduced the sound transmission level by 25-35 dB within the 1- 5 kHz frequency range and by 15-30 dB within the 0.5-1kHz range, performing better than a conventional double-pane IGU by 5-10 dB within the entire studied range of sound frequencies.

Accelerated durability testing showed no detectable degradation, indicating anticipated lifetime of at least 20 years (fig. S21B, tables S6 and S7) (*24*), comparable to that of conventional IGUs. Because MOCHI can be confined between panes of glass, replacing air of conventional double-pane windows, or adhered to protective hard plastic films in retrofits, the window product durability was further enhanced by the glass or plastic confinement. However, even unprotected MOCHI exhibit good durability under conditions expected for air-purifying disposable windows (fig. S23) (*24*). Indeed, one of the reasons for selecting polysiloxane (silicone) in our MOCHI designs was that it is already widely used in edge sealing of commercial windows.

The combination of visible-range transparency and thermal insulation is of interest for many applications beyond windows. In one example (Fig. 4), we show how it allows for solar thermal

energy harnessing, with the potential utility in compensating for the energy still leaking through building envelopes. By encasing a broadband blackbody solar absorber with our MOCHI effectively transmitting solar but blocking thermal-infrared radiation (Fig. 4A, figs. S25 and S26), we can entrap the absorbed solar thermal energy that can be then used for needs like heating water or building interior (Fig. 4B-D). This energy harnessing yields high stagnation temperatures ~300 ºC of the absorber for both solar simulator and ambient conditions (Fig. 4B). At the high temperatures of blackbody receiver, the blackbody radiation spectrum shifts to shorter wavelengths, where MOCHI become semi-transparent (Fig. 4C, figs. S25 and S26). Therefore, differently from the ambient temperatures case, the radiative heat transfer becomes important at high stagnation temperatures of the blackbody receiver, causing some heat loss (Fig. 4D). While one can modify MOCHI to make them more opaque in the range 3-6 μm (fig. S26A) to further boost the solar thermal energy harnessing, the demonstrated stagnation temperatures (Fig. 4B) are the highest temperatures achieved for unconcentrated solar radiation, to the best of our knowledge. The harnessed thermal energy can be channeled for heating building interior or water using heat exchangers. Importantly, harnessing can be done even on a cloudy day, when ambient solar energy is at ~0.3 sun, which could be particularly advantageous in cold climates, Small parts of the opaque component of the building envelope could become solar heat-based power generators capable of reducing the overall building energy consumption (Fig. 4E and F).

Discussion

In order to assess the potential impact of using MOCHI in building envelopes, we have performed EnergyPlus simulations to estimate the energy saving with the help of MOCHI-IGUs and solar thermal energy generation that could replace other energy sources used for heating and cooling the building interior, like electricity and gas (*24*). The wall-grade efficient MOCHI-IGUs would allow for increasing the fraction of building envelopes occupied by windows, potentially boosting the windows area from the current 8% to 30% while actually reducing the energy wasted for heating (Fig. 3I, figs. S27 and S28). The global variations of solar thermal energy generation per square-meter of MOCHI-based solar thermal panel are shown in Fig. 4E, which can be converted into interior-heating or solar-thermal-powered cooling (*26*) energy or water heating. Typically, solar thermal panels covering a fraction of a single-family-home's opaque envelope would be sufficient to meet the heating and cooling needs, as illustrated for US states in Fig. 4F. Having larger areas of solar thermal harnessing panels would then generate energy beyond building's heating and cooling needs, converting it into an energy generating plant.

To conclude, we developed MOCHI metamaterials with high transparency and lower than still air's thermal conductivity, comparable to that of aerogels used in the Mars Rover (*4-12*). Cold-temperature insulation of MOCHI-IGUs stopped 95% of heat transfer, making windows as insulated as high-performing building walls. Self-assembly-based fabrication and optical-contact-enabled scaling of MOCHI slabs and films with diverse geometric form-factors is suitable for applications in building envelope. Our MOCHI can expand the use of insulated glazing in envelopes of future buildings, including in windows, skylights and porous-material-based daylighting (*27,28*). While silicone-based sealants are already widely used in IGUs, our MOCHI could replace the conventional gas fillers with "frozen air" nanosponge-like methyl-silicone-based fillers. Potential applications may extend to greenhouse coverings, protective and heat-insulating apparel (*29*), space exploration (*15*), whenever simultaneous optical transparency and thermal insulation are needed. MOCHI can be surface-functionalized or modified by adding nanoparticles (*30*) to achieve custom-designed properties ranging from solar gain control to air purification (*31*), potentially including disposable insulating air-cleaning windows (*24*).

References and Notes

1. F. Trubiano, *Design and Construction of High-performance Homes: Building Envelopes, Renewable Energies and Integrated Practice* (Taylor and Francis, 2013).
2. J. Lovell, *Building Envelopes: An Integrated Approach (Architecture Briefs)* (Princeton Architectural Press, 2010).
3. J. L. Aguilar-Santana, H. Jarimi, M. Velasco-Carrasco, S. Riffat, Review on window-glazing technologies and future prospects. *Int. J. Low-Carbon Technol.* **15**, 112–120 (2020).
4. I. I. Smalyukh, Thermal management by engineering the alignment of nanocellulose. *Adv. Mater.* **33**, 2001228 (2020).
5. M. K. Carroll, A. M. Anderson, S. T. Mangu, Z. Hajjaj, M. Capron, Aesthetic aerogel window design for sustainable buildings. *Sustainability* **14**, 2887 (2022).
6. C. Buratti, E. Belloni, F. Merli, M. Zinzi, Aerogel glazing systems for building applications: a review. *Energy Build.* **231**, 110587 (2021).
7. E. Belloni, C. Buratti, F. Merli, E. Moretti, T. Ihara, Thermal-energy and lighting performance of aerogel glazing with hollow silica: field experimental study and dynamic simulations. *Energy Build.* **243**, 110999 (2021).
8. Q. Liu, I. I. Smalyukh, Liquid crystalline cellulose-based nematogels. *Sci. Adv.* **3**, e1700981 (2017).
9. R. Hart, S. Selkowitz, C. Curcija, Thermal performance and potential annual energy impact of retrofit thin-glass triple-pane glazing in US residential buildings. *Build. Simul.* **12**, 79–86 (2019).
10. T. Shimizu, K. Kanamori, A. Maeno, H. Kaji, and K. Nakanishi, Transparent ethylene-bridged polymethylsiloxane aerogels and xerogels with improved bending flexibility. *Langmuir* **32**, 13427–13434 (2016).
11. E. Abraham, V. Cherpak, B. Senyuk, J. B. ten Hove, T. Lee, Q. Liu, I. I. Smalyukh, Highly transparent silanized cellulose aerogels for boosting energy efficiency of glazing in buildings. *Nat. Energy* **8**, 381–396 (2023).
12. Y. Kobayashi, T. Saito, A. Isogai, Aerogels with 3D ordered nanofiber skeletons of liquid-crystalline nanocellulose derivatives as tough and transparent insulators. *Angew. Chem. Int. Ed.* **53**, 10394–10397 (2014).
13. L. Zhao, E. Strobach, B. Bhatia, S. Yang, A. Leroy, L. Zhang, E.N. Wang. Theoretical and experimental investigation of haze in transparent aerogels. *Opt. Express* **27**, A39−A50 (2019).
14. Q. Liu, A. W. Frazier, X. Zhang, J. A. De La Cruz, A. Hess, R. Yang, I. I. Smalyukh, Flexible transparent aerogels as window retrofitting elements with tunable birefringence. *Nano Energy* **48**, 266–272 (2018).
15. R. Wordsworth, L. Kerber, C. Cockell, Enabling Martian habitability with silica aerogel via the solid-state greenhouse effect. *Nat. Astron.* **3**, 898–903 (2019).

16. B. Fleury, E. Abraham, J. A. De La Cruz, V. S. Chandrasekar, B. Senyuk, Q. Liu, V. Cherpak, S. Park, J. B. ten Hove, I. I. Smalyukh, Aerogel from sustainably grown bacterial cellulose pellicles as a thermally insulative film for building envelopes. *ACS Appl. Mater. Interfaces* **12**, 34115–34121 (2020).

17. C.-S. Ha, S. S. Park, *Periodic Mesoporous Organosilicas: Preparation, Properties and Applications*, vol. 281 in Springer Series in Materials Science (Springer, ed.1, 2019).

18. C. T. Kresge, M. Leonowicz, W. J. Roth, J. C. Vartuli, J. S. Beck, Ordered mesoporous molecular sieves synthesized by a liquid-crystal template mechanism. *Nature* **359**, 710–712 (1992).

19. K. M. McGrath, D. M. Dabbs, N. Yao, I. A. Aksay, S. M. Gruner, Formation of a silicate L3 phase with continuously adjustable pore sizes. *Science* **277**, 552–556 (1997).

20. C. P. Singh, M. Yousuf, S. B. Qadri, D. C. Turner, B. P. Gaber, B. R. Ratna, Transparent monolithic cubic mesoporous silica synthesized by structure-directing surfactant. *Appl. Phys. A* **77**, 585–589 (2003).

21. S. H. Tolbert, A. Firouzi, G. D. Stucky, B. F. Chmelka, Magnetic field alignment of ordered silicate-surfactant composites and mesoporous silica. *Science* **278**, 264–268 (1997).

22. K. M. McGrath, D. M. Dabbs, N. Yao, K. J. Edler, I. A. Aksay, S. M. Gruner, Silica gels with tunable nanopores through templating of the L3 phase. *Langmuir* **16**, 398–406 (2000).

23. M. Kruk, M. Jaroniec, V. Antochshuk, A. Sayari, Mesoporous silicate-surfactant composites with hydrophobic surfaces and tailored pore sizes. *J. Phys. Chem. B* **106**, 10096–10101 (2002).

24. Materials and methods are available as supplementary materials.

25. R. Mitchell, C. Kohler, D. Curcija, L. Zhu, S. Vidanovic, S. Czarnecki, D. Arasteh, J. Carmody, C. Huizenga, WINDOW 7 User Manual (Lawrence Berkeley National Laboratory, 2019); https://windows.lbl.gov/window-documentation

26. C.A. Balaras, G. Grossman, H.-M. Henning, C.A. Infante Ferreira, E. Podesser, L. Wang, E. Wiemken. Solar air conditioning in Europe - an overview. *Renewable and Sustainable Energy Reviews* **11**, 299-314 (2007).

27. M. Ganobjak, W. J. Malfait, J. Just, M. Käppeli, F. Mancebo, S. Brunner, J. Wernery, Get the light and keep the warmth - A highly insulating, translucent aerogel glass brick for building envelopes. *J. Build. Eng.* **64**, 105600 (2023).

28. K. McEnaney, L. Weinstein, D. Kraemer, H. Ghasemi, G. Chen, Aerogel-based solar thermal receivers. *Nano Energy* **40**, 180-186 (2017).

29. F. Azam, F. Ahmad, Z. Ulker, M. S. Zafar, S. Ahmad, A. Rasheed, Y. Nawab, C. Erkey, The role and applications of aerogels in textiles. *Adv. Mater. Sci. Eng.* **1**, 2407769 (2022).

30. Q. Liu, H. Mundoor, G. H. Sheetah, I. I. Smalyukh, Plasmonic gold-cellulose nanofiber aerogels. *Opt. Express* **28**, 34237-34245 (2020).

31. S. Hu, C. Li, K. Li, W. Teng, F. Li, P. Zhang, H. Wang, Advanced mesoporous adsorbents and catalysts for CO_2, NO_x, and VOC removal: mechanisms and applications. *Environ. Sci.: Nano* **11**, 4666-4691 (2024).

32. D. Chateau, A. Liotta, F. Vadcard, J. R. G. Navarro, F. Chaput, J. Lermé, F. Lerouge, S. Parola, From gold nanobipyramids to nanojavelins for a precise tuning of the plasmon resonance to the infrared wavelengths: experimental & theoretical aspects. *Nanoscale* **7**, 1934-1943 (2015).
33. J. R. Kremer, D. N. Mastronarde, J. R. McIntosh, Computer visualization of three-dimensional image data using IMOD. *J. Struct. Biol.* **116**, 71-76 (1996).
34. J. B. ten Hove, F. W. van Leeuwen, A. H. Velders, Manipulating and monitoring nanoparticles in micellar thin film superstructures. *Nat. Commun.* **9**, 5207 (2018).
35. D. N. Mastronarde, Automated electron microscope tomography using robust prediction of specimen movements. *J. Struct. Biol.* **152**, 36-51 (2005).
36. M. Kruk, M. Jaroniec, Gas adsorption characterization of ordered organic− inorganic nanocomposite materials. *Chem. Mater.* **13,** 3169-3183 (2001).
37. S. Lowell, J. E. Shields, M. A. Thomas, M. Thommes, *Characterization of Porous Solids and Powders: Surface Area, Pore Size and Density* (Springer, 2004).
38. M. Born, E. Wolf, *Principles of Optics* (Cambridge Univ. Press, ed. 7, 1999).
39. M.P. Keating, *Geometric, Physical & Visual Optics* (Butterworth–Heinemann, ed. 2, 2002).
40. R. W. G. Hunt, M. R. Pointer, *Measuring Colour* (John Wiley & Sons, ed. 4, 2011).
41. R. Dangol, T. Kruisselbrink, A. Rosemann, Effect of window glazing on colour quality of transmitted daylight. *J. Daylighting* **4**, 37–47 (2017).
42. Y. Ohno, Color rendering and luminous efficacy of white LED spectra. *Proc. SPIE* **5530**, 88-98 (2004).
43. Y. Ohno, Spectral design considerations for color rendering of white LED light sources. *Opt. Eng.* **44**, 111302 (2005).
44. Glass in building—Determination of light transmittance, solar direct transmittance, total solar energy transmittance, ultraviolet transmittance & related factors. ISO 9050:2003 (2003).
45. T. M. Tritt, *Thermal Conductivity: Theory, Properties, and Applications* (Kluwer Academic/Plenum Publishers, 2004).
46. C. Buratti, E. Belloni, L. Lunghi, M. Barbanera, Thermal conductivity measurements by means of a new 'Small Hot-Box' apparatus: manufacturing, calibration and preliminary experimental tests on different materials. *Int. J. Thermophys.* **37**, 47 (2016).
47. C. Buratti, E. Moretti, E. Belloni, M. Zinzi, Experimental and numerical energy assessment of a monolithic aerogel glazing unit for building applications. *Appl. Sci.* **9**, 5473 (2019).
48. W.R. McCluney, *Encyclopedia of Energy Engineering & Technology* (CRC Press, ed.2, 2014).
49. Voluntary test method for thermal transmittance and condensation resistance of windows, door and glazed wall sections. AAMA 1503-09 (2009).
50. X. Zhang, F. Shi, J. Niu, Y. Jiang, Z. Wang, Superhydrophobic surfaces: from structural control to functional application. *J. Mater. Chem.* **18**, 621-633 (2008).
51. A. F. Konstantinova, B. N. Grechushnikov, B. N. Bokut', and Y. G. Valyashko, *Optical Properties of Crystals* (Nauka i Tekhnika, Minsk, 1995).

52. E. Charlet, E. Grelet, Anisotropic light absorption, refractive indices, and orientational order parameter of unidirectionally aligned columnar liquid crystal films. *Phys. Rev. E* **78**, 041707 (2008).

53. Y. Li, P. Zhang, G. Chen, Y. Li, W. Hua, Y. Li, Z. Jiao, Study on method for measuring coating emissivity by applying active irradiation based on infrared thermal imager. *Sensors (Basel)* **22**, 2392 (2022).

54. Y. Meng, J. Xue, R. Han, T. Xu, Y. Ding, Y. Yang, Preparation, design, structure and application of aerogel-based materials for noise control. *J. Mater. Sci.* **60**, 383–413 (2025).

55. A.J.B. Tadeu, D. M.R. Mateus, Sound transmission through single, double and triple glazing. Experimental evaluation, *Applied Acoustics* **62**, 307-325 (2001).

56. L. Zhao, B. Bhatia, S. Yang, E. Strobach, L.A. Weinstein, T.A. Cooper, G. Chen and E.N. Wang. Harnessing Heat Beyond 200 °C from Unconcentrated Sunlight with Nonevacuated Transparent Aerogels. *ACS nano* **13**, 7508−7516 (2019).

57. C. Buratti, E. Moretti, E. Belloni, Nanogel windows for energy building efficiency, *Nano and biotech based materials for energy building efficiency,* (Springer International publishing, 2016, pp. 41–69).

58. N. Bheekhun, A.R. Abu Talib, M.R. Hassan, Aerogels in aerospace: An Overview. *Adv. Mater. Sci. Eng.* **1**, 406065 (2013).

59. T. Gao, T. Ihara, S. Grynning, B.P. Jelle, A.G. Lien, Perspective of aerogel glazings in energy efficient buildings. *Build. Environ.* **95,** 405–413 (2016).

60. https://www.energy.gov/eere/buildings/articles/ultra-clear-aerogels-insulated-glass-refrigeration-doors

61. https://www.buildinggreen.com/blog/r-10-vacuum-insulated-glazing

62. https://www.vacuum-glass.com/vacuum-insulating-glass-price-costs/?amp=1

Acknowledgments: We thank B. Borak, K. Burrows, J. Cameron, J. De La Cruz, T. Culp, C. Fitz, J. Gerbi, A. Hess, M. Krarti, M. Lafrance, Q. Liu, P. de Melo, S. Mumme, E. Schiff, M. Sofos, R. Tenent, T. White and Y. Yuan for discussions. We are grateful to F. Leresche for discussions and the use of a solar simulator, as well as H. Zhao and R. Fei for technical assistance.

Funding: We acknowledge support of the US Department of Energy, under the Advanced Research Projects Agency-Energy (ARPA-E) award DE-AR0000743, during which the development of MOCHI was initiated (J.-B.t.H., E.A., V.C., B.S., T.L., B.F. and I.I.S.). We also acknowledge the DOE EERE grant DE-EE0009699 that supported the development of thick slabs of MOCHI and highly insulating glass units based on them (A.B., E.A., B.S., T.L and I.I.S.). We acknowledge the CU BEST center for the partial support of solar thermal energy harnessing part of this work (A.B. and I.I.S.).

Author contributions:

Conceptualization: IIS

Methodology: AB, BF, BS, EA, JBtH, TL, VC, IIS

Investigation: AB, BF, BS, EA, JBtH, TL, VC, IIS

Funding acquisition: IIS

Project administration: IIS

Supervision: IIS

Writing – original draft: AB, BS, EA, JBtH, TL, IIS

Writing – review & editing: AB, BF, BS, EA, JBtH, TL, VC, IIS

Competing interests: Authors filed patent applications related to MOCHI technology; additional patent applications were filed concurrently with the submission of this manuscript.

Data and materials availability:

All data are available in the main text or in the supplementary materials. Information requests should be directed to the corresponding author.

Supplementary Materials

Materials and Methods

Supplementary Text

Figs. S1 to S28

Tables S1 to S7

References (*32-62*)

Movies S1 to S10

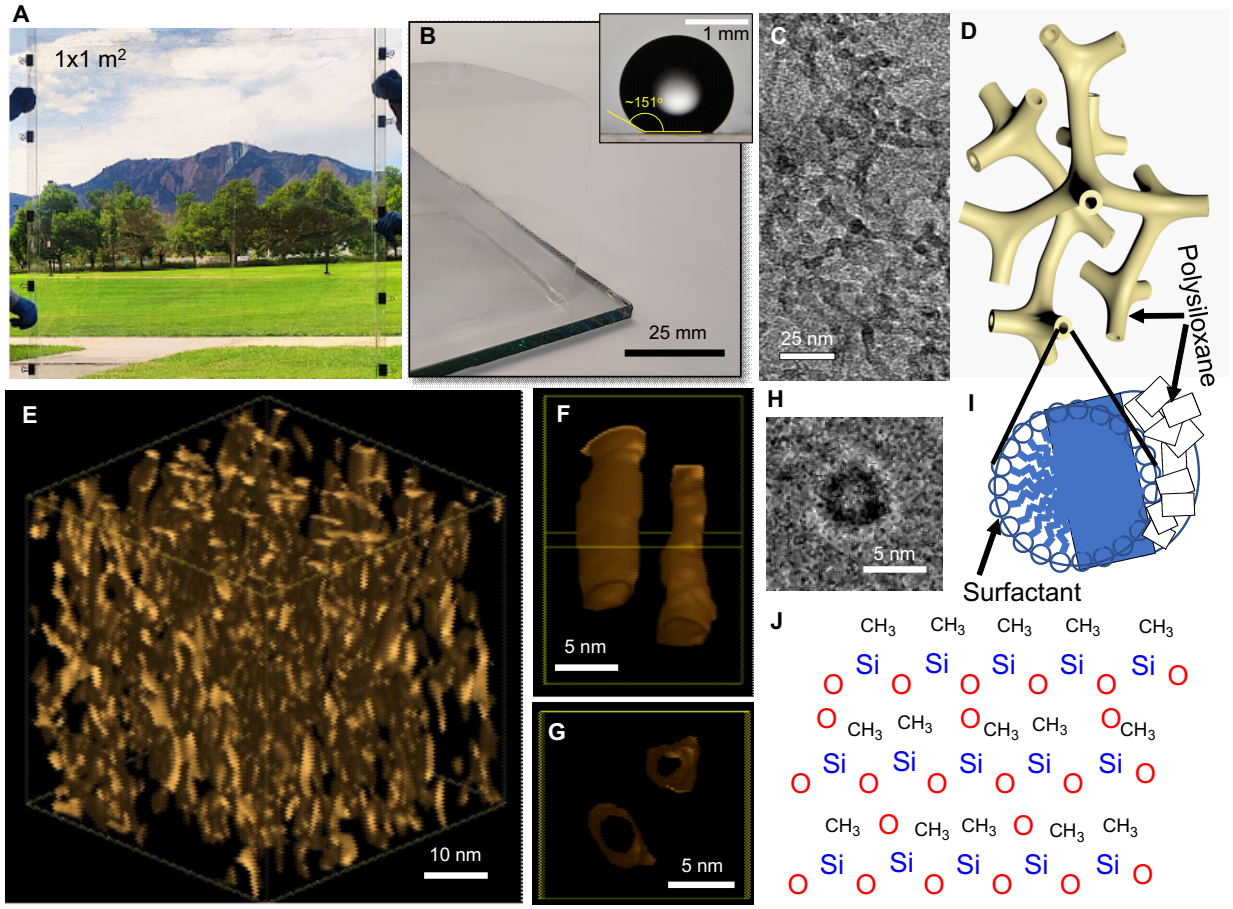

Fig. 1. Large-scale MOCHI metamaterials and their nanoscale morphology. (**A**) Optical photograph illustrating high transparency of a square-meter retrofit with 3-mm-thick MOCHI atop of a plastic film. (**B**) A corner perspective view of a 5-cm-thick highly transparent MOCHI slab atop of a glass plate. The inset displays a water droplet atop of MOCHI, with a large contact angle highlighting super-hydrophobicity (*24*). (**C**) TEM image of a MOCHI, revealing the graph-like networks. (**D**) Corresponding schematic illustration of the nanotube graph network. (**E**) TEM tomographic reconstruction of the nanoscale morphology of MOCHI, demonstrating the orientationally orderly arrangement of hollow polysiloxane tubes within a graph-like network. (**F** and **G**) Zoomed-in tomographic reconstructions of two individual nanotubes viewed from mutually orthogonal perspectives. (**H**) TEM image of an edge-on-oriented polysiloxane tube templated by a cylindrical micelle of surfactant molecules, as shown in the schematic (**I**). (**J**) Polysiloxane network within the walls of nanotubes.

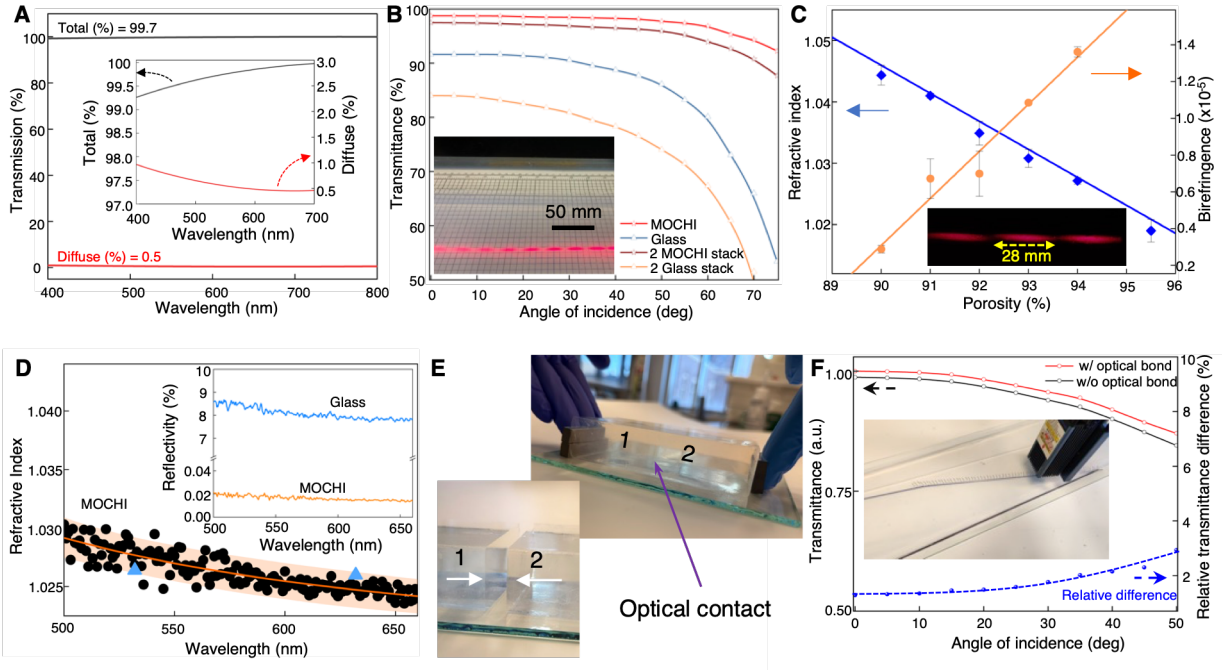

Fig. 2. Optical properties of MOCHI. (**A**) Total and diffuse transmission of MOCHI versus wavelength, showing a high average transparency of 99.7% with haze <1%. Inset shows details of these dependencies. (**B**) Angular dependencies of transmittance for thin MOCHI films for a single and double-stacked MOCHI films as compared to glass counterparts, demonstrating >90% transmittance even at high incidence angles. The inset shows laser light propagation through monocrystal-like monolithic MOCHI, with the periodic scattered light modulation arising from its birefringence properties. (**C**) Refractive index and birefringence versus porosity of MOCHI. Circular and diamond symbols show experimental data; orange line is based on linear fitting. The refractive index dependence was fit (blue line) with a Arago-Biot relation averaging refractive indices of silica (1.457) and air (1.0003) at 632 nm, weighted by their volume fractions (*24*). The inset shows a zoomed-in view of modulated scattering laser light traversing through the metamaterial, on a dark background. (**D**) Variation of the average effective refractive index of MOCHI within the visible spectrum, derived from spectral reflectivity measurements. The inset compares the spectral dependencies of reflectivity of MOCHI and glass; blue triangles show the data points from independent measurements using laser light (*24*). (**E**) Photographs showing two inch-thick MOCHI slabs achieving optical contact upon being pressed toward each other; photographs were taken under illumination optimized to allow visibility of slabs that are generally "invisible" due to weak surface reflections and transparency. (**F**) Normalized transmittance of MOCHI slabs in (E), before and after optical bonding for different incidence angles, indicating the relative transmittance improvement upon bonding. The inset shows laser cutting multi-centimeter-thick MOCHI slab placed atop of glass, defining the shape printed on a white underneath.

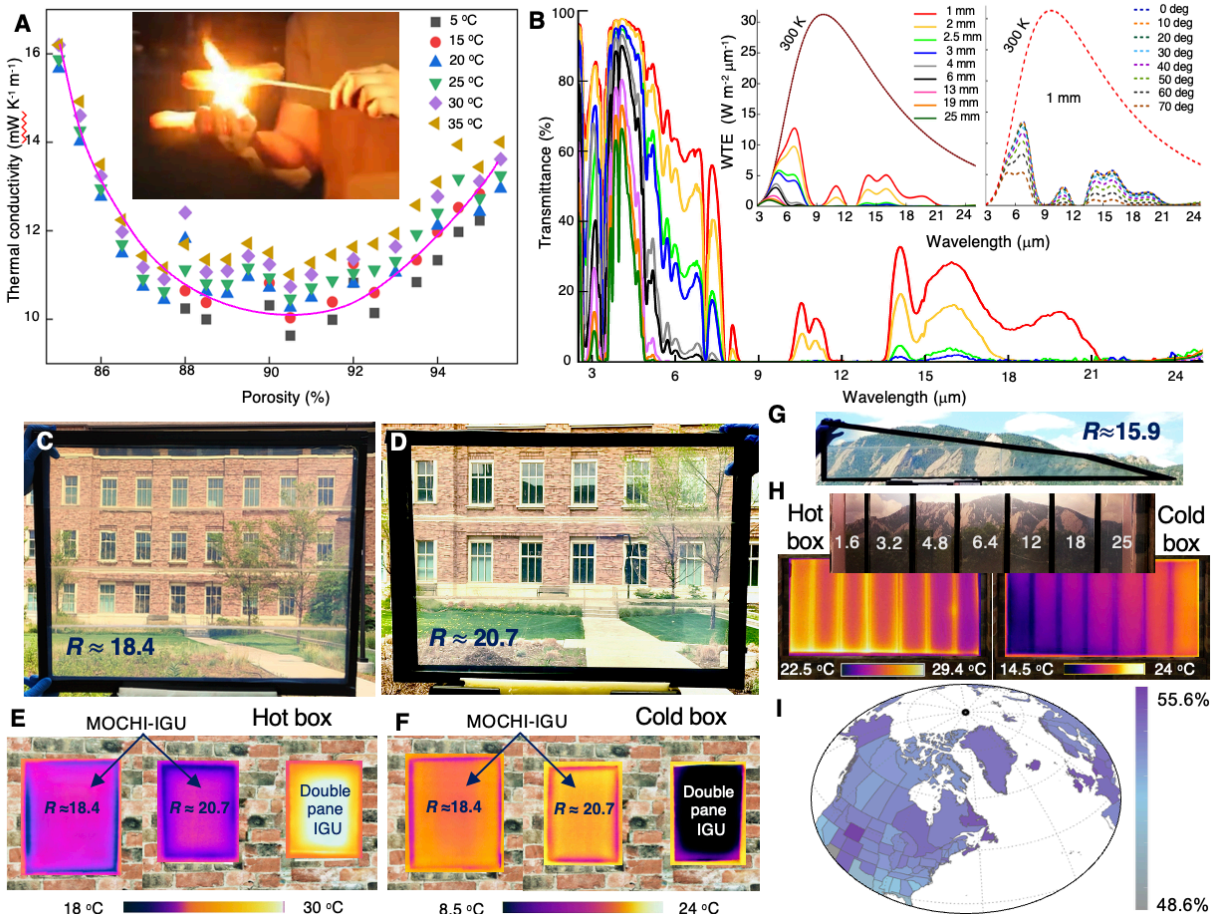

Fig. 3. Thermal barrier properties and impact of using MOCHI in insulating glass units. (**A**) Thermal conductivity of MOCHI versus porosity at different temperatures. A magenta solid line is an eye guide. Inset highlights the fire retardancy and thermal super-insulation of a MOCHI film while protecting from flame (video S1), allowing for safe on-hand barbecuing. (**B**) Thermal infrared transmittance for MOCHI of varying thickness. Insets show the weighted infrared transmissive emittance (WTE) per μm-unit wavelength (*24*) for blackbody radiation at 300 K, for MOCHI versus thicknesses (left) and versus light's incidence angle for 1-mm-thick MOCHI (right). (**C** and **D**) Optical photographs illustrating high transparency and color rendering of MOCHI-IGUs: (**C**) 52.5cm × 65cm of 35mm thickness with $R \approx 3.24$ m^2 K W^{-1}, (**D**) 35cm × 50cm of 37.5 mm thickness with $R \approx 3.65$ m^2 K W^{-1} (*24*), as measured for external and internal temperatures of -4 °C and 16 °C, respectively. (**E** and **F**) Thermal photographs of MOCHI-IGUs shown in C and D as compared to that of a conventional double pane IGU with an air gap of 12 mm, in both (E) hot box (at 40 °C) and (F) cold box (-10 °C) environments. (**G**) Optical photograph of a complex-shaped MOCHI-IGU with lateral dimensions 127.5cm × 25cm and thickness 37.5 mm having $R \approx 2.8$ m^2 K W^{-1} (*24*). *R*-values marked in (C-G) are in the units of h ft^2 °F Btu^{-1}. (**H**) Optical and thermal images for MOCHI slabs with varying thickness, ranging from 1.6 mm to 25 mm, where the latter are taken above hot and cold boxes at temperatures of 40 °C and -10 °C, respectively. (**I**) Global map of percentage of building's heating and cooling energy savings enabled by MOCHI-IGUs replacing single-pane windows, averaged over a year, as estimated for a standard single-family home (*24*).

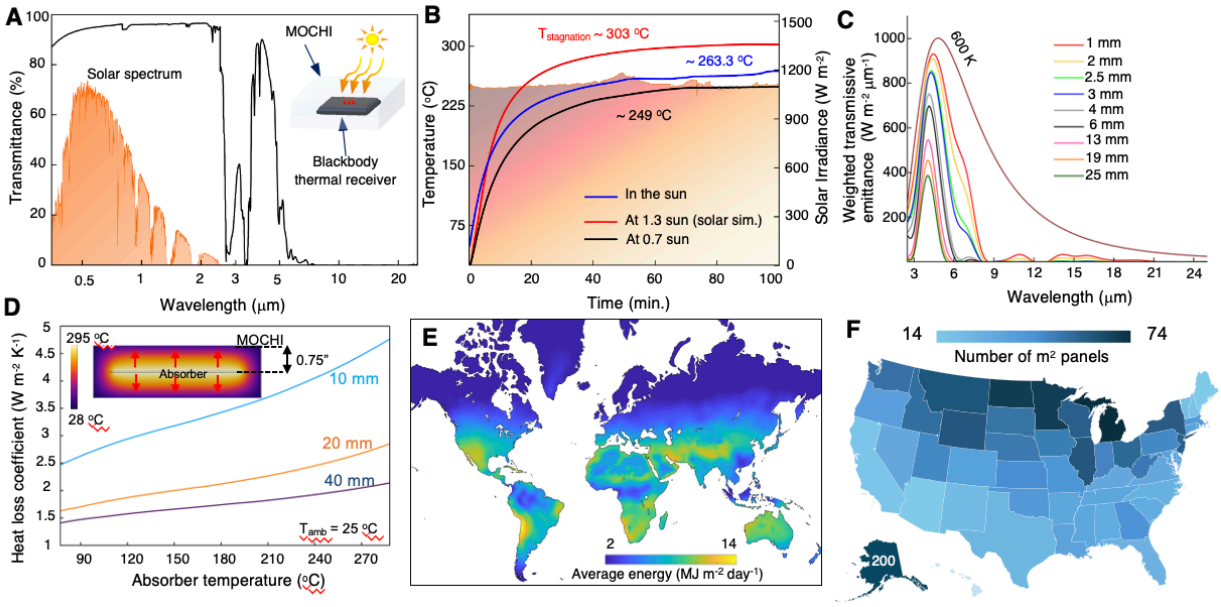

Fig. 4. Solar thermal energy harnessing enabled by MOCHI. (**A**) Spectral transmittance of a MOCHI slab (black curve) showing high transparency in visible and near-infrared ranges, which correspond to solar radiation spectrum (orange) at Earth's surface, along with strong absorption in the part of thermal infrared range >5 μm. (**B**) Stagnation temperatures of a blackbody thermal receiver at various irradiation intensities obtained under ambient conditions (for monitored solar radiation intensity) and using a solar simulator, as schematically shown in the inset of (A) (*24*). (**C**) The weighted transmissive emittance per μm-unit wavelength (*24*), weighted by 600 K blackbody radiation, for MOCHI slabs of different thicknesses. (**D**) Heat loss coefficient of the solar thermal harnessing system for MOCHI slabs of different thickness. Inset shows the heat escape from absorber via MOCHI. (**E**) Annual average energy generated by a solar thermal panel per square meter per day mapped throughout the world based on the average solar irradiation (*24*). (**F**) A map showing the number of square-meter panels required to meet heating and cooling energy needs for single-family homes in the US, simulated with EnergyPlus based on the geographical location and average annual energy consumption (*24*).